

Spectroscopy and Computations of Supported Metal Adducts. 1. DFT Study of CO and NO Adsorption and Coadsorption on Cu/SiO₂

Piotr Pietrzyk

Faculty of Chemistry, Inorganic Chemistry Department, Jagiellonian University, R. Ingardena 3, 30-060 Cracow, Poland

Received: February 17, 2005; In Final Form: March 18, 2005

Interactions of the CO and NO molecules with the Cu^{II} and Cu^I isolated sites on the amorphous silica surface are investigated by means of density functional theory (DFT) methods within the finite cluster model approach. The clusters of silica of increasing **nT** size (**T** = Si) are used, with **n** from 2 to 6. The Cu^{II} sites are characterized by calculated **g**-tensors and hyperfine coupling constants (HFCCs) and compared with experiment. On this basis, the three-coordinated complexes are the most plausible. Due to the charge transfer from the silica “ligand”, the metal charge shrinks and the spin density is distributed over silanol and siloxy groups up to 50%. The reduced sites are exclusively two-coordinated. Strong interaction of CO with Cu^I–**nT** sites (31–39 kcal/mol) gives rise to the formation of carbonyl adducts with planar coordination around copper. The population of the ligand π^* system shifts downward the stretching frequency in agreement with experiment. Reaction with a second CO molecule gives a geminal dicarbonyl of very uniform structure independent of the site. Carbonyl complexes with Cu^{II} are less stable and of tetrahedral coordination of the metal. Accumulation of the positive charge on the complex along with σ overlap with d orbitals locates the calculated CO stretching frequency above free molecule value. NO molecule is preferably bound to the Cu^{II}–**nT** sites, forming a tetrahedral complex with tilted adsorbate and NO stretching frequency blue-shifted with respect to the free molecule value. The full set of electron paramagnetic resonance (EPR) parameters and vibrational frequencies for the copper(I) mononitrosyl, {CuNO}¹¹, though not observed experimentally, are predicted and compared to the same magnetophore inside the ZSM-5 zeolite. The interaction energies show that in the CO/NO reaction mixture adsorption is selective and allows discrimination between Cu^I and Cu^{II} sites. However, for the Cu^I complex, formation of mixed-ligand structures of the {Cu(CO)(NO)}¹¹ type is possible.

1. Introduction

Many practical catalysts consist of one or several catalytically active components deposited on a high-surface-area support, for example, high-surface silica, alumina, zeolites, aluminosilicates, or active carbon. Among them, silica is an amorphous system inert in most catalytically relevant processes. Chemical reactions occurring at the surfaces of such materials have received great interest because of their importance in a variety of fields including atmospheric chemistry, heterogeneous catalysis and photocatalysis, corrosion science, environmental chemistry, metallurgy, soil science, and biology.¹

CO and NO molecules are common reactants in many chemical processes. Reactions involving carbon monoxide, a most suitable synthon, have been the subject of many studies. They concern both homogeneous catalysis (e.g., hydroformylation of olefins and amination of CO and carbonyl compounds)² and heterogeneous catalysis (e.g., oxidation of CO from exhaust gas, steam reforming, water-gas shift reaction, methanol synthesis, and CO hydrogenation).³ Reactions involving, in turn, the interaction of nitric oxide with transition-metal ions (TMIs) have received ongoing interest, since they are of fundamental importance in inorganic and biological nitrogen cycles.^{4,5} Significant effort has been made to develop biomimetic systems capable of activating the nitric oxide molecule. In this context, the synthesis of inorganic catalysts based on high-surface silica or aluminosilicates, that contain isolated surface TMIs as active

redox sites, has been used for developing new types of catalysts.⁶ A longstanding issue has been devoted to a design of the active and selective catalysts applicable to *de*NO_x processes.⁴

In all of the above-mentioned reactions, heterogeneous copper systems have been recognized as active catalysts and some recent practical uses of the Cu/SiO₂ system in promoting methanol steam reforming⁷ or selective hydrogenation of alkynes into alkenes⁸ motivate ongoing works. However, despite numerous efforts, little is still known about the nature of the Cu⁺ and Cu²⁺ sites deposited on high-surface supports. Experimental difficulties in direct refinement of their local structure stem mainly from a low content of copper, profound speciation, and irregular geometries often encountered in disordered systems or at surfaces, which lead to low-symmetry environments. Thus, spectroscopic methods (indirect), for example, the electron paramagnetic resonance (EPR), IR, Raman, or extended X-ray absorption fine structure (EXAFS) (averaging) methods, combined with molecular modeling and prediction of spectroscopic parameters of adopted models may be a powerful tool for describing the active sites.

Silica as a support and the silica-supported catalysts have been extensively investigated by means of experimental and computational tools. In particular, copper–silica systems of various stenochemical factors were reported, for example, amorphous catalyst,⁹ meso-^{10,11} and macroporous¹² materials, and composite nanowires.¹³ A vast panoply of spectroscopic and surface science methods was used to study the valence state of copper¹⁴ and its interaction with the support,¹⁵ distribution, and particle size,^{16,17} as well as the coordination sphere of copper complexes support-

* Fax: (+48 12) 634 05 15. Phone: (+48 12) 663 22 24. E-mail: pietrzyk@chemia.uj.edu.pl.

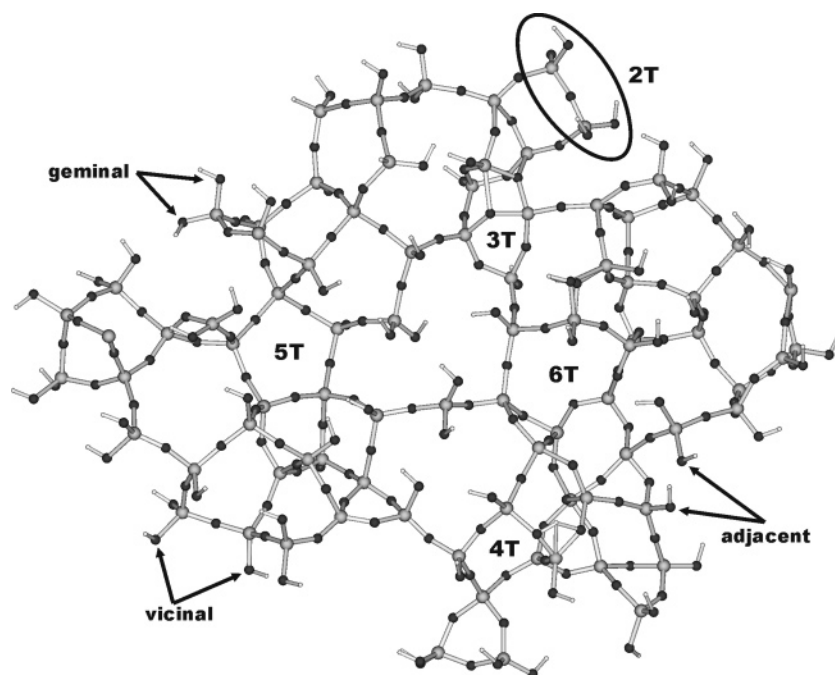


Figure 1. Structure of the amorphous silica surface obtained from molecular dynamic simulation. The various types of silanol groups are indicated along with the ringlike structures used for the construction of the nT clusters.

TABLE 1: Physicochemical Methods Used for the Characterization of Silica-Supported Copper Cu/SiO₂

spectroscopy	analysis	results	ref
DR UV-vis	symmetry	distorted octahedral and tetrahedral species	18
EPR	symmetry	three-coordinated mononuclear and distorted tetrahedral Cu ^{II} surface complex	18,19
	electronic ground state	$d_{x^2-y^2}$ ($S = 1/2$)	17–19
	spin state	isolated Cu ^{II} ($S = 1/2$) (major species), ion pairs ($S = 1$)	18
EXAFS	local surroundings	Cu–O distance 1.94–1.97 Å	18, 20
		Cu–Si distance 2.6–3.5 Å	18, 20
		Cu–Cu distance 2.62 Å	20
IR	frequency of adsorbed molecular probes (CO, NO)	existence of Cu ^{II} , Cu ^I , and Cu ⁰ species	23, 24
XPS	valence state, dispersion of active phase	mutual presence of Cu, CuO, and Cu ₂ O clusters under oxidizing conditions	14

ed on silica.^{18–20} Another strategy is based on the use of molecular probes where the status of the metal center is elucidated on the basis of the structure and reactivity of adsorption complexes formed. The main interest in this research context is devoted to IR spectroscopy of the adsorption of CO^{21–25} and NO.^{24–26} The spectroscopic characterization of the Cu/SiO₂ system is summarized in Table 1. One point needs a comment here. The surface of the Cu/SiO₂ catalysts prepared by grafting, impregnation, or sol–gel methods after thermal treatment in a vacuum exhibits mainly the isolated sites for low coverage (the maximum capacity of the silica surface calculated from the density of the OH groups has been estimated to be between 5 and 10 wt % Cu¹⁹). The samples referred to in Table 1 (diffuse reflectance spectroscopy DRS, IR, and EPR experiments) are around 1 wt % and below. Ion pairs observed by EPR have been claimed to be the minor species and are easily destroyed by readmission of air into the sample. They have not been restored after further evacuation.¹⁸ The EXAFS data reporting the presence of the Cu–Cu pairs at a distance of 2.62 Å have been obtained for as prepared, not calcined samples.²⁰ The authors interpreted the dimers as two aqua complexes with one H₂O ligand exchanged for a siloxy group in each.

In parallel, quantum chemistry can provide detailed information about microscopic aspects of the interaction of metal with support and adsorbents (e.g., CO and NO). From the literature, the surface of amorphous silica has emerged as a subject of

various computational approaches. The bulk structure of silica, apart from stishovite and silica W, consists of SiO₄ tetrahedra covalently linked to each other through oxygen atoms. The various crystalline and amorphous forms of silica differ only in the arrangement of the SiO₄ unit.²⁷ One of the possibilities relies on the structure of β -cristobalite. Some X-ray diffraction (XRD) works have shown the existence of a local order which resembles that of β -cristobalite and related crystalline phases.²⁸ The surface is heterogeneous and most probably composed of regions of partially hydroxylated (100) and (111) β -cristobalite surfaces.²⁹ This model has been used to predict oxygen-bridged Os and Rh surface carbonyl complexes²⁹ and periodic trends in the interaction of first-row transition metals with a silica surface.³⁰ The structure and reconstruction of silica have been studied in this manner using large models such as slabs, chains, ring, and cages involving hybrid quantum mechanics/molecular mechanics^{31,32} and periodic plane-wave density functional theory (DFT)^{30,33,34} methods. On the other hand, silica surface models established by molecular dynamics offer a variety of surface siloxane and silanol ligands (only two types of such groups are present in the above-mentioned crystalline-type model) and a much more heterogeneous and flexible surface that resembles real vitreous silica more likely.^{35,36} This model gives an advantage of cutting off small clusters mimicking local sites of various sizes on the surface.³⁷ TMI surface complexes and their adsorption adducts have been studied using the cluster

approach,^{38–40} and in particular, they have been used for modeling copper–silica complexes.^{32,41,42}

The structure of an amorphous silica surface obtained by molecular dynamics simulation is presented in Figure 1. The most characteristic feature of such a surface is the presence of a large variety of (SiO)_n cycles and several types of silanol groups. Among them, geminal OH groups located on the same silicon, vicinal silanol groups (Si–OH) bonded through one siloxane bridge (Si–O–Si), and adjacent Si–OH groups linked by two consecutive siloxane bridges are visible.

The present paper deals with the theoretical characterization of isolated surface complexes of Cu^I and Cu^{II} ions grafted on silica, that would correspond to the low surface coverage of the metal, and identification of their adsorption complexes with CO and NO molecules. In light of the lack of direct structural data, the computational results allow us to design proxies of the species formed during the carbonylation and nitrozylation reactions. The aim is to analyze and assign frequencies and spin-Hamiltonian parameters by comparing the available experimental data for the adsorption and coadsorption of CO and NO on Cu/SiO₂. Proper prediction of the spectroscopic parameters of surface complexes, for example, *g*-tensor, hyperfine coupling constants, harmonic frequencies, and energy of d–d transitions, can be regarded as a reliable test of the adequacy of adopted geometrical models as well as of a calculation scheme itself. Since, for many reasons, there is no one-to-one and onto correspondence between the structure and the spectrum, prediction of spectral features and their corroboration with experimental counterparts enhances, on one hand, the robustness of the approach and, on the other hand, gives direct quantitative insight into details of the geometrical and electronic structure. Hereafter, such a procedure is taken as a paradigm in this series.

2. Computational Methods

The results of spectroscopic investigations (see Table 1) are quite scattered, suggesting pronounced speciation of the Cu^{II} and Cu^I centers on the amorphous silica surface. This situation calls for the calculation of Cu/SiO₂ models of various quantum cluster sizes exhibiting various types of oxygen ligands. In the present work, isolated centers are considered and the silica surface is modeled with clusters of increasing number of silicon atoms. The broken bonds of the clusters have been saturated by H atoms, a commonly adopted technique to embed clusters of covalent materials.⁴³ Numerous studies have shown that silica can be considered as a covalent oxide characterized by localized two-centered bonds. In this respect, introduction of the long-range Madelung potential is much less important than it is in other ionic oxides. Although the cluster modeling takes into account only the surface atoms lying close to the metal, it has the advantage to perform high-level calculations that result in a precise local picture of the studied site in terms of the geometry and spectroscopic features.⁴⁴

Geometry optimization has been carried out by means of DMol⁴⁵ software developed by Accelrys Inc.,⁴⁶ with no symmetry restrictions, at the spin unrestricted level. Thus, when discussing one-electron energy levels, the SOMO and LUMO terms are considered in the sense of the highest occupied and the lowest unoccupied spin-orbital in the spin majority manifold, respectively. As the exchange-correlation potential, the generalized gradient approximation (GGA) of Becke⁴⁷ and Perdew and Wang⁴⁸ has been utilized. The double numerical basis set supplemented by polarization functions (DNP) has been used. The cluster models have been fully optimized without any constraints starting from various initial structures using analytic gradients and the BFGS method.⁴⁹ The results have not been

corrected for basis set superposition error. The self-consistent field (SCF) electron density convergence criterion of 10^{–6} au has been set. The criterion for optimal geometry is based on the gradient and displacement norm values and energy value for which thresholds of 10^{–3}, 10^{–3}, and 10^{–5} au have been used, respectively. The vibrational analysis has been performed using the harmonic approximation. The Hessian matrices have been evaluated by numerical differentiation (one-point finite difference) of the analytic energy gradients using a displacement of 0.01 bohr from the optimized geometry for all 3N coordinates. Charge distribution has been obtained from Hirshfeld (“stockholder”) partitioning⁵⁰ of molecular one-electron density recommended for numerical DFT calculations. Bond order analysis has been achieved according to the Mayer scheme.⁵¹

The hyperfine splitting has been calculated for the previously optimized geometries with the Gaussian03⁵² package. The combination of the BPW91 exchange-correlation functional with the 6-311G(df) and LanL2DZ basis sets has been used, as justified in the earlier work.⁴⁴ As for the *g*-tensor calculations, the ADF suite,^{53,54} version 2002.03, has been employed. The *g*-tensors have been obtained by the UKS-Pauli approach using gauge-including atomic orbitals.⁵⁵ Since the *g*-tensors for many transition-metal complexes were shown to be essentially independent of the choice of density functional,⁵⁵ we applied the VWN LDA method. An all-electron triple- ζ Slater-type basis set with a set of polarization functions has been used.

To be directly compared to the IR results, the calculated at the BPW/DNP level harmonic frequencies are corrected by a scaling factor (XY_{exptl}/XY_{DFT}) taking into account the anharmonicity. For the stretching mode, this factor is derived from the free CO and NO molecules, since it fits the experimental data well.⁵⁶ The ratio of the experimental frequency to the computed harmonic one for the CO molecule is 2143/2108 = 1.017, and for the NO molecule, it is 1876/1843 = 1.018.

3. Results and Discussion

3.1. Model Clusters. The clusters modeling sites of the silica surface used in this work have been cut off from the molecular dynamics (MD) model of SiO₂ (Figure 1) so that they would represent various types of the rings existing on the surface, as well as the surface silanol groups. They are referred to according to the nomenclature used in zeolite chemistry, where the size of the ring is denoted by the number of **T** atoms (**T** = Si or Al) except oxygen atoms. The constructed clusters allow mimicking of the 3-fold coordination of Cu^{II} ions, as suggested by the experimental measurements (Table 1), but 2-fold and 4-fold coordination are also considered.

The simplest model of a silica framework is a corner-shared two-silicon tetrahedral structure, [Si₂O₂(OH)₅][–], which will be referred to as **2T**. It represents the situation of vicinal siloxy (SiO[–]) and silanol (Si–OH) groups linked by the Si–O–Si bridge. In particular, this type of cluster has already been used to model silica-supported Cu³² and Mo ions.³⁸ The cluster [Si₃O₄(OH)₅][–] referred to as **3T** is the simplest ringlike model. This six-membered ring exhibits two silanol groups and one siloxy group. The cluster is terminated with OH groups. The **4T** model, [Si₄O₅(OH)₇][–], exhibits three silanols and one siloxy group and can act as a tetradentate surface ligand while all Si atoms are terminated with OH. Saturation of one of the silicon atoms by hydrogen atoms enforces tridentate character of the cluster, and this situation has been also examined afterward. The **4T** model has been used in an earlier study of the structure and reactivity of silica and zeolite catalysts.³¹ The 10-membered ring referred to here as **5T** has the chemical composition of

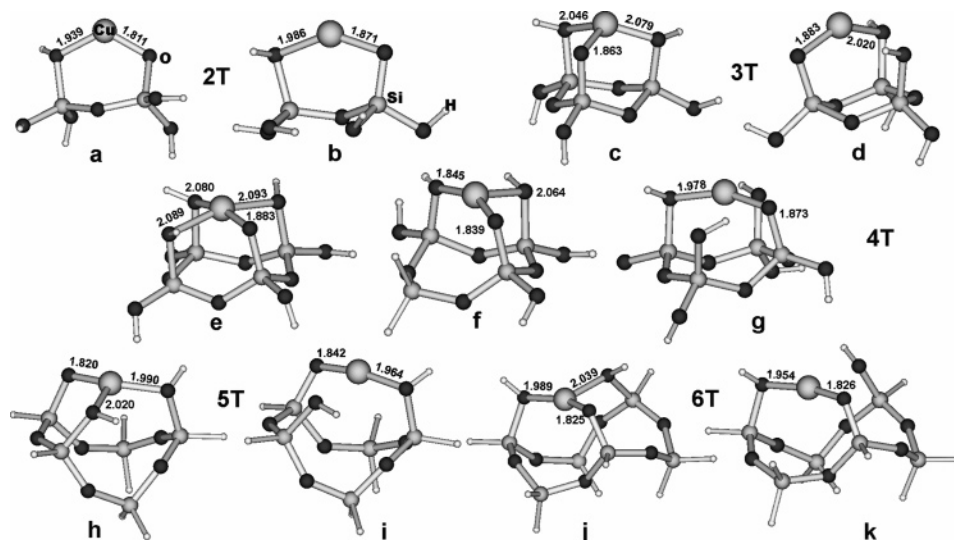


Figure 2. Optimized structures of the copper surface complexes of increasing silica cluster size. Structures a, c, e, f, h, and j represent $\text{Cu}^{\text{II}}-\text{nT}$ sites, while structures b, d, g, i, and k show $\text{Cu}^{\text{I}}-\text{nT}$ (for details, see text). The Cu–O bond lengths are given in angstroms.

$[\text{Si}_5\text{O}_6(\text{OH})_2\text{H}_7]^-$. It can act as a tridentate surface ligand with its two adjacent silanol groups and a silanolate group. The big size of the model makes it very flexible and has allowed confirming successfully the properties of $\text{Ni}^{\text{II}}_{3\text{c}}$ ions grafted on silica with comparison to EXAFS data.³⁹ In this study, the gallery of silica models has been extended over an even bigger cluster, namely, **6T**, of chemical formula $[\text{Si}_6\text{O}_7(\text{OH})_2\text{H}_9]^-$. Such a 12-membered structure can also be distinguished on the amorphous silica surface (Figure 1). The silicon atoms of the **5T** and **6T** models have been saturated by hydrogens in order to reduce their size.

After incorporation of Cu^{I} and Cu^{II} cations into the silica models, the $\text{Cu}^{\text{I}}-\text{nT}$ surface complexes remain neutral while the $\text{Cu}^{\text{II}}-\text{nT}$ ones are all +1 charged. Enduring the same silica models regardless of the charge of the ion allowed checking the influence of a valence state of Cu on the properties of surface adducts without changing the ligands around the metal. The alternative would be to place two siloxy groups in the case of the Cu^{II} complex, but this involves changing the surroundings by replacing one silanol by one siloxy group which have appeared to be nonequivalent ligands throughout this study. In real materials, the compensation of charge generated by the $(\text{Cu}^{\text{II}}-\text{silica})^+$ sites would be possible by the counterions from the copper precursors used during the synthesis (for “wet” samples) or the dissociated silanol groups in the vicinity of the copper clusters. The presence of siloxy groups is not surprising, since the grafting of copper to the surface undergoes in the basic medium. The calcination of a sample carried out under high-outgassing-temperature conditions maintains a considerable dehydroxylation of the surface and prevents the protonation.

3.2. Structure of Cu/SiO_2 Sites. The optimized geometries of the Cu^{II} and Cu^{I} ions hosted in **nT** ($n = 2, 3, 4, 5, 6$) sites are presented in Figure 2 along with the selected population analysis data collected in Table 2: total copper valence, sum of the O–Cu–O angles ($\Sigma\angle\text{O}-\text{Cu}-\text{O}$), partial charge on copper (Q_{Cu}), copper spin density (ρ_{Cu}), and HOMO energy level (ϵ_{HOMO}). Divalent copper sites can be grouped into three generic types of structures: (i) two-coordinated $\text{Cu}^{\text{II}}_{2\text{c}}-\text{2T}$ (Figure 2a), (ii) three-coordinated $\text{Cu}^{\text{II}}_{3\text{c}}-\text{3T}$, **4T**, **5T**, and **6T** (Figure 2c,f,h,j), and (iii) four-coordinated $\text{Cu}^{\text{II}}_{4\text{c}}-\text{4T}$ (Figure 2e). This classification is supported by the values of the copper total valence indices listed in Table 2. Various coordinations of Cu^{II} cations have also been confirmed theoretically in zeolites, for

TABLE 2: Adsorption Properties of Cu^{II} and Cu^{I} Ions on the Silica Surface

cluster	total Cu valence	$\Sigma\angle\text{O}-\text{Cu}-\text{O}$ (deg)	Q_{Cu} (au)	ρ_{Cu} (au)	ϵ_{HOMO} (eV)
$\text{Cu}^{\text{II}}-\text{2T}$	1.90	124	0.60	0.38	−11.889
$\text{Cu}^{\text{II}}-\text{3T}$	2.07	327	0.55	0.48	−11.281
$\text{Cu}^{\text{II}}_{4\text{c}}-\text{4T}$	2.64	355	0.50	0.49	−10.804
$\text{Cu}^{\text{II}}_{3\text{c}}-\text{4T}$	2.38	346	0.50	0.44	−11.301
$\text{Cu}^{\text{II}}-\text{5T}$	2.38	356	0.48	0.45	−11.163
$\text{Cu}^{\text{II}}-\text{6T}$	2.43	360	0.49	0.48	−10.820
$\text{Cu}^{\text{I}}-\text{2T}$	1.40	142	0.28	0	−5.855
$\text{Cu}^{\text{I}}-\text{3T}$	1.42	139	0.29	0	−5.773
$\text{Cu}^{\text{I}}-\text{4T}$	1.58	156	0.29	0	−5.935
$\text{Cu}^{\text{I}}-\text{5T}$	1.52	166	0.25	0	−5.539
$\text{Cu}^{\text{I}}-\text{6T}$	1.54	165	0.25	0	−5.494

example, in A and Y,⁵⁷ where a six-membered ring can behave as a tri- or tetradentate “ligand” depending on the number of aluminum atoms substituted. The bond lengths between copper-(II) and siloxy ligands turn up in the range 1.811–1.883 Å, while for the silanols this distance is distinctly longer and appears in the range 1.939–2.093 Å. The sum of the angles between these bonds ($\Sigma\angle\text{O}-\text{Cu}-\text{O}$) gives insight into the planarity of the copper environment. For the ringlike clusters, only the $\text{Cu}^{\text{II}}-\text{3T}$ complex shows distinctly pyramidal structure, whereas the $\text{Cu}^{\text{II}}-\text{4T}$, $\text{Cu}^{\text{II}}-\text{5T}$, and $\text{Cu}^{\text{II}}-\text{6T}$ clusters are nearly planar considering copper first coordination sphere. The calculated average Cu–Si distances ($\langle d_{\text{Cu}-\text{Si}} \rangle$) for the optimized sites are equal to 2.972 Å for **2T**, 2.919 Å for **3T**, 2.935 Å for **4T**, 3.034 Å for **5T**, and 3.095 Å for **6T** and are in good agreement with experimental EXAFS data. The same is valid for the calculated Cu–O distance values which come out within experimental range (for both, see Table 1).

Planar coordination of Cu^{II} ions leads to maximization of the σ interaction between the Cu $d_{x^2-y^2}$ and oxygen ligands. The Cu–O binding has thus a partially covalent nature, as evidenced by the charge distribution in Table 2. The more planar copper surroundings, the more covalent bonding, and the lower copper partial charge (Q_{Cu}) have been obtained. In general, the positive charge of copper shrinks upon adsorption on silica due to considerable charge transfer from silanol and siloxy ligands to the metal. A similar effect of the lattice has been observed for zeolites.⁵⁸ Nearly 50% of the spin density (ρ) is localized on copper with the exception of $\text{Cu}^{\text{II}}-\text{2T}$, where $\rho_{\text{Cu}} = 38\%$. The shape of the spin density and the corresponding SOMO contour

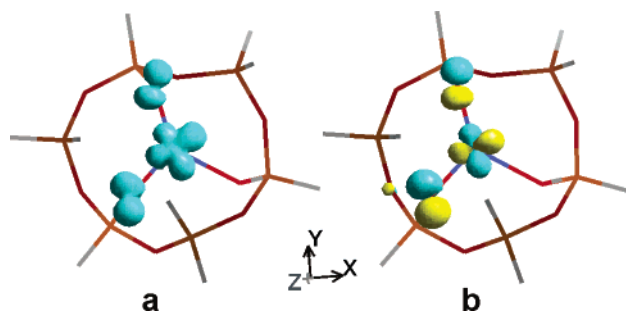


Figure 3. The spin density (a) and SOMO (b) contours for the Cu^{II}–6T complex.

TABLE 3: Electronic *g*-Tensor Values Calculated for Cu^{II}–Silica Surface Complexes

cluster	<i>g</i> ₁₁	<i>g</i> ₂₂	<i>g</i> ₃₃
Cu ^{II} –2T	2.210	2.187	2.044
Cu ^{II} –3T	2.656	2.106	1.972
Cu ^{II} _{4c} –4T	2.160	2.045	2.039
Cu ^{II} _{3c} –4T	2.243	2.086	2.047
Cu ^{II} –5T	2.218	2.115	2.054
Cu ^{II} –6T	2.243	2.081	2.040
experimental ^{17,18}	2.36	2.07	2.07
	2.53	2.13	2.04

for the Cu^{II}–6T structure is shown in Figure 3 as an example. This result can be taken as a rule for all calculated Cu^{II}–silica structures in this study, indicating the *d_{x²–y²}* ground state in agreement with the EPR results.¹⁸

Upon reduction, the status of the copper ions has changed significantly. Regardless of the hosting site, the structures are exclusively two-coordinated and the total copper valence index decreases by about 30%. With the decrease of the coordination number (CN), the overall average Cu–O distance decreases slightly also, that is, $\langle d_{\text{Cu–O}} \rangle = 1.943$ Å for Cu^{II}–5T and 1.903 for Cu^I–5T. In the case of the highly unsaturated 2T site, the CN is preserved independent of the oxidation state. The corresponding values are equal to 1.875 and 1.929 Å, respectively.

To test the quality of the Cu^{II}–silica proxies, the computed *g*-tensors have been corroborated with the available EPR data. The experimental results are somewhat scattered, showing the Cu(II) surface species of both axial and rhombic symmetry (Table 3). Moreover, the spectra have not been simulated and the quoted data are not computer-fitted values which make them of limited confidence. Nevertheless, some features are characteristic. First of all, the $g_{\text{iso}} = 1/3(g_{11} + g_{22} + g_{33})$ value is greater than *g_e* for all optimized structures, that is characteristic for Cu(II) species,⁵⁹ following the pattern $g_{11} \gg g_{22} \approx g_{33}$. Second, *g*₁₁ has the biggest value due to magnetic-field-induced coupling of the occupied *d_{x²–y²}* SOMO (Figure 3) and occupied *d_{xy}* orbital.

The calculated values listed in Table 3 are very similar for all structures, but the best agreement with experiment is achieved for the Cu^{II}–3T complex. Note that this structure exhibits pronounced nonplanarity of the copper surroundings. The similar results have been reported on Cu^{II} sites in mordenite.⁶⁰ In the regular E site, the *g*_{||} value has been found to be between 2.27 and 2.30, while, in the trigonal coordination with one hydroxyl ligand, the *g*_{||} value has been around 2.40. For the Cu^{II}–2T cluster, the only one with CN = 2, the particular components (*g_{ii}*) are too small and follow a different pattern: $g_{11} \approx g_{22} \gg g_{33}$. The site 4T, displayed in Figure 2e,f, has allowed for examination of the influence of CN on *g_{ii}*. Even though this effect is small, it is clear that the Cu^{II}_{3c} structure has bigger *g*-tensor components than the Cu^{II}_{4c} structure, thus more similar to the experimental ones.

The presented results are based on the Ziegler–Schreckenbach method employing the Pauli Hamiltonian. To make sure that this method is adequate, the newest implementation of the ZORA Hamiltonian, that allows unrestricted calculations in collinear approximation, has been tested. The ZORA unrestricted *g*-tensor results for the 5T and 6T sites are equal to [2.240; 2.076; 2.025] and [2.297; 2.062, 2.013], respectively, and show only moderate influence expressed by a slight increase of particular *g_{ii}* values.

The hyperfine coupling constant (HFCC) tensor is less informative than the *g*-tensor in this case. Due to the large line widths and the structural disorder of the powder samples, the complete hyperfine splitting is hardly ever observed. Generally, for axial signals, the parallel component (*A*_{||}) lies in the range 122–180 G¹⁸ and the perpendicular component (*A*_⊥) is not resolved. The performance of the 6T site has been tested, and the hyperfine coupling constants [*A*₁₁], [*A*₂₂], and [*A*₃₃] are equal to 115.9, 75.7, and 98.7 G, respectively. For the pyramidal structure of the Cu^{II}–3T complex, the respective *A*-tensor components are the following: [*A*₁₁] = 118.2 G, [*A*₂₂] = 10.7 G, and [*A*₃₃] = 73 G. The calculated hyperfine tensors exhibit rhombic symmetry, which is typical for a low-symmetry environment imposed by a surface. EPR spectra of such symmetry have been observed for dehydrated Cu/SiO₂ catalyst,¹⁸ unfortunately without hyperfine splitting.

3.3. Adsorption of CO on Cu/SiO₂. **3.3.1. Structure of Adducts.** There is now a consensus that in copper complexes CO is bonded via σ bond and π back-bond. The HOMO orbital of CO is the 5 σ^* antibonding orbital. σ overlap with the appropriate orbitals of the TMI would strengthen both the CO bond and the Cu–CO interaction. On the other hand, the LUMO of CO is the 6 π^* orbital. The electron flow from the symmetry allowed d orbitals to the LUMO would strengthen the Cu–CO interaction but weaken the CO bond. As a result, a delicate balance between these two mechanisms governs the observed frequency shifts of CO which, in turn, is considered as a criterion for dividing copper carbonyls into two groups: high-frequency, nonclassical carbonyl complexes of Cu⁺ in zeolites²¹ and low-frequency, classical carbonyl complexes of bulk Cu(0)²² and oxide-supported copper.²⁴ The notation of Enemark and Feltham⁶¹ is used throughout this study, where {Cu(XY)_{*m*}}^{*n*} stands for the complex with the sum of copper d electrons and π^* electrons of the XY ligand equal to *n*.

The coordination of a CO molecule to Cu^I/SiO₂ has been exoenergetic with the adsorption energy (ΔE_{ads}) ranging from –39.8 to –30.6 kcal/mol for the Cu^I–6T and Cu^I–4T sites, respectively. Similar values have been reported recently for Cu⁺/MFI zeolite.⁶² The structures of {CuCO}¹⁰–silica adsorption complexes are shown in Figure 4a,c,e,g,i, and selected bonding parameters are summarized in Table 4. ΔQ_{Cu} and ΔQ_{CO} stand for a change of the partial charge of copper and CO, respectively, with respect to a bare copper–silica site and a free CO molecule. CO appears to be a powerful ligand that is able to reconstruct the coordination sphere of Cu^I. Geometry optimization led to the almost linear η^1 –C adducts (the corresponding Cu–C–O angle values are in the range 176–178°) with Cu–C bond lengths (*d*_{Cu–C}) of approximately 1.79–1.80 Å. The concomitant deformation of the Cu bonding to the silica framework upon CO adsorption consists both of the change of CN and changes in Cu–O bond lengths. Depending on the cluster, ligation of CO occurs with the conservation of the total coordination number of copper as the new Cu–C link is formed with the expense of the former Cu–OHSi bond (2T and 3T structures) or with the increase of the CN of Cu from 2 to 3

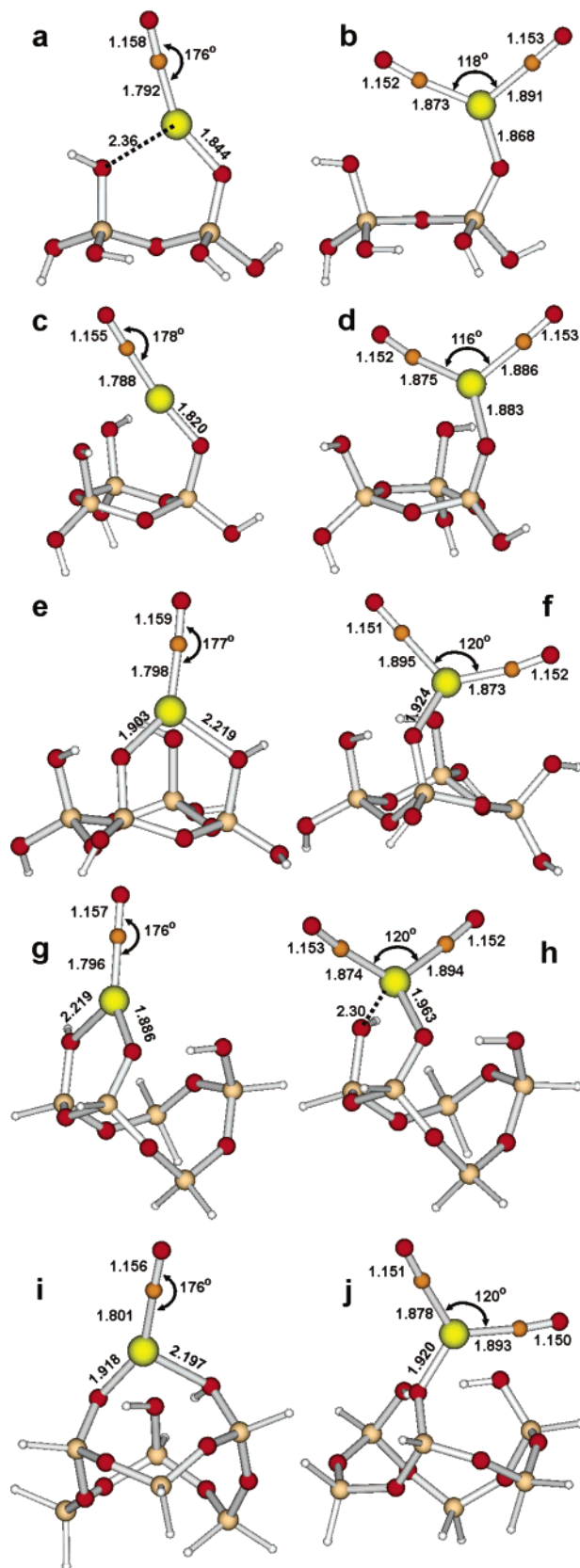


Figure 4. Structures of the monocarbonyl $\{\text{CuCO}\}^{10}$ (left column) and dicarbonyl $\{\text{Cu}(\text{CO})_2\}^{10}$ (right column) adsorption complexes nested in **2T** (a and b), **3T** (c and d), **4T** (e and f), **5T** (g and h), and **6T** (i and j) sites. All bond lengths are given in angstroms, and angles, in degrees.

(**4T**, **5T**, and **6T**). The reason for such a behavior might be the size of the hosting site. The biggest site, the highest flexibility of the complex, and the least dramatic changes in the geometry

after reaction with adsorbate could be expected. Surface carbonyl complexes bonded via only one siloxy group have already been described by Pakkanen et al. in the example of the $\text{Co}(\text{CO})_n/\text{silica}$ system.⁶³ The interaction of cobalt polycarbonyls with SiO^- has appeared stronger than that with nonbridging oxygen or hydroxylated surface sites. In the case of increasing CN, the average Cu–O distance increases also from $\langle d_{\text{Cu-O}} \rangle = 1.903$ to 2.053 Å (illustrative values for the **5T** cluster). Even though the bond between copper and the silanol group in the $\{\text{CuCO}\}^{10}$ –**2T** structure is relatively long (see Figure 4a), the carbonyl moiety is more similar to the ones of three-coordinated copper adducts (Figure 4e,g,i). This is indicated mainly by similar C–O and Cu–C bond lengths and Cu total valence listed in Table 4.

Adsorption of a CO molecule on the $\text{Cu}^{\text{II}}/\text{SiO}_2$ leads to the formation of $\{\text{CuCO}\}^9$ –silica adducts, whose optimized molecular models are shown in Figure 5a–c and briefly characterized in Table 5. The adsorption is exoenergetic, but the ΔE_{ads} values strongly depend on the cluster size. For the biggest clusters, **5T** and **6T**, the results are converged to a reasonable limit. This limit is more than 2 times lower than the ΔE_{ads} value for copper-(I) sites that supports observation derived from the IR experiments about low stability of the $\{\text{CuCO}\}^9$ adducts in comparison to the $\{\text{CuCO}\}^{10}$ ones. The $\{\text{CuCO}\}^9$ unit exhibits a nearly linear η^1 –C structure with the average C–O bond lengths shorter by about 0.012 Å than those assessed for $\{\text{CuCO}\}^{10}$ clusters. On the contrary, the average Cu–C bond lengths are longer by 0.090 Å. Adsorption on the Cu^{II} –**5T** and Cu^{II} –**6T** sites leads to the tetragonal coordination of copper, but $\langle d_{\text{Cu-O}} \rangle$ is increased by 0.231 Å (for the **5T** structure) in comparison to bare copper clusters. In the case of the smaller **3T** site, the Cu–C link is formed at the expense of one of the copper–silanol bonds.

Upon successive interaction of $\{\text{CuCO}\}^{10}$ –**nT** with a second CO molecule, dicarbonyl complexes of the $\{\text{Cu}(\text{CO})_2\}^{10}$ type are formed. This type of surface complexes has been observed on the amorphous silica surface^{11,24} as well as within zeolite channels.^{21,64} Moreover, homogeneous copper(I) polycarbonyls have also been reported.⁶⁵ The strong trans influence of the CO ligand removes another silanol ligand from the coordination sphere of copper that results in the very uniform type of adducts: geminal $\{\text{Cu}(\text{CO})_2\}^{10}$ moieties with two linearly bonded CO molecules attached by one copper–siloxy link to the silica cluster. The dicarbonyl structures are illustrated in Figure 4b,d,f,h,j. The adsorption energy of the second CO molecule (between –6.0 kcal/mol for **2T** and –10.2 kcal/mol for **5T**) is rather small, but regarding the structural and population analysis data, both CO ligands appear to be equivalent. Much lower adsorption energies suggest that the transformation of the monocarbonyls to dicarbonyls occurs after complete saturation of the adsorption sites by one CO molecule. The ratio of the number of Cu^{I} sites occupied by one CO molecule (N_{CO}) to the number of the sites with two CO molecules ($N_{(\text{CO})_2}$) at 298 K is equal to 10^{16} , as calculated from the ΔE_{ads} value for the Cu^{I} –**5T** complex according to the Boltzmann distribution. Thus, at first, ligation of only one molecule occurs, and afterward, the second CO molecule can be bound providing sufficiently high pressure of the adsorbate. Regardless of the cluster, the bond lengths of CO ligands turn up in the narrow range 1.150–1.153 Å and the angle (θ) between CO molecules is close to 120°. The respective angle (θ) for intrazeolitic complexes assessed from their IR spectra has been equal to 130°. The wider span of the Cu–O bond lengths equal to 1.912 ± 0.095 Å does not influence the geometry of the $\{\text{Cu}(\text{CO})_2\}^{10}$ moiety much. In conclusion, adsorption of the second CO molecule averages local surround-

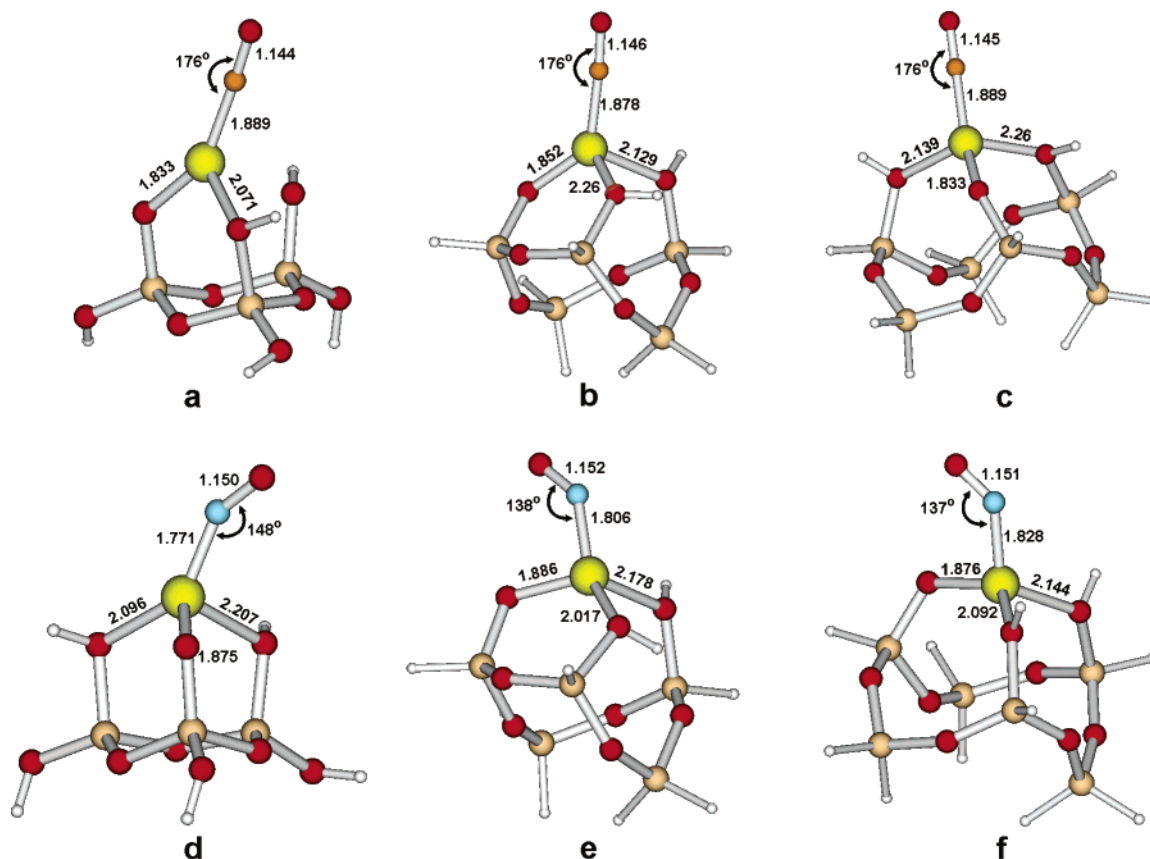


Figure 5. Comparison of the structures of the {CuCO}⁹ adsorption complexes in the 3T site (a), 5T site (b), and 6T site (c) with the structures of the {CuNO}¹⁰ adsorption complexes in the 3T site (d), 5T site (e), and 6T site (f). All bond lengths are given in angstroms, and angles, in degrees.

TABLE 4: Comparison of CO Bond Lengths, Adsorption Energies, and Selected Population Analysis Data for Cu^I Monocarbonyl {CuCO}¹⁰ Adducts

	structure				
	{CuCO} ¹⁰ –2T	{CuCO} ¹⁰ –3T	{CuCO} ¹⁰ –4T	{CuCO} ¹⁰ –5T	{CuCO} ¹⁰ –6T
ΔE_{ads} (kcal/mol)	–35.0	–35.2	–30.6	–31.6	–39.8
ΔQ_{Cu}	0.043	0.027	0.029	0.082	0.090
ΔQ_{CO}	0.025	0.057	0.021	0.035	0.042
d_{CO}^a (Å)	1.158	1.155	1.159	1.157	1.156
C–O bond order ^b	2.312	2.334	2.313	2.319	2.322
Cu–C bond order	1.186	1.164	1.162	1.157	1.135
Cu total valence	2.380	2.268	2.426	2.344	2.275

^a To be compared with 1.151 Å for a free CO molecule. ^b To be compared with a 2.495 bond order for free CO.

TABLE 5: Comparison of CO Bond Lengths, Adsorption Energies, Selected Population Analysis Data, and CO Stretching Frequency for Cu^{II} Monocarbonyl {CuCO}⁹ Adducts

	structure			
	{CuCO} ⁹ –2T	{CuCO} ⁹ –3T	{CuCO} ⁹ –5T	{CuCO} ⁹ –6T
ΔE_{ads} (kcal/mol)	–30.9	–28.8	–16.1	–13.4
ΔQ_{Cu}	–0.122	–0.095	–0.077	–0.069
ΔQ_{CO}	0.204	0.200	0.166	0.166
d_{CO}^a (Å)	1.144	1.144	1.146	1.145
C–O bond order ^b	2.442	2.444	2.424	2.429
Cu–C bond order	0.916	0.902	0.919	0.901
Cu total valence	2.722	2.762	2.857	2.876
ν (cm ^{–1}) (int. km/mol)	2191 (606.37)	2198 (534.42)	2174 (706.57)	2177 (546.30)
ν_{CO} experimental ^c	2200–2208			

^a To be compared with 1.151 Å for a free CO molecule. ^b To be compared with a 2.495 bond order for free CO. ^c Experimental data taken from ref 24.

ings of copper cation and leads to the disappearance of the speciation observed among monocarbonyl adducts.

3.3.2. IR Spectrum of Adducts. The most important feature of the interaction of the Cu^I/SiO₂ with CO that can be obtained

from experiment is the frequency of adsorbed CO. Contrary to the {CuCO}¹⁰ in zeolites, for example, ZSM-5,²¹ the copper(I) carbonyls supported on silica show peaks in the range 2135–2122 cm^{–1}, which are slightly red-shifted from the peak at 2143

TABLE 6: Calculated CO Stretching Frequency of Mono- and Dicarboxyl Adducts for Various Cu^I–Silica Cluster Models

structure	{CuCO} ¹⁰	{Cu(CO) ₂ } ¹⁰	
	ν (cm ⁻¹) (int. km/mol)	ν_{symm} (cm ⁻¹) (int. km/mol)	ν_{asymm} (cm ⁻¹) (int. km/mol)
Cu ^I – 2T	2114 (597.6)	2144 (286.0)	2103 (733.9)
Cu ^I – 3T	2138 (542.3)	2148 (297.9)	2110 (675.2)
Cu ^I – 4T	2113 (587.5)	2150 (277.7)	2113 (630.7)
Cu ^I – 5T	2121 (601.5)	2144 (308.6)	2105 (658.9)
Cu ^I – 6T	2120 (630.2)	2159 (285.9)	2122 (607.2)
experimental	2122, 2126, 2132 ^a	2163	2128
	2115, 2128, 2135 ^b	2162	2129

^a From ref 24, amorphous silica as a support. ^b From ref 11, mesoporous MCM-41 silica as a support.

cm⁻¹ of the gas-phase CO. This downward shift should correspond to the weaker and longer CO bond, as can be seen in Table 4. To confirm this observation, the stretching frequency of adsorbed CO has been calculated and the results are collected in Table 6. The red shift is reproduced correctly, and the values of the CO stretching frequency are very close to that observed experimentally. The calculated values are slightly scattered ($\Delta\nu = 25$ cm⁻¹) which could reflect the heterogeneity of Cu^I centers, as indicated by the three different CO stretching frequencies in IR data. The highest frequency is observed for the structure where only one siloxy group participates in bonding with the {CuCO}¹⁰ moiety (**3T**). As can be seen in Table 4, such a structure has the lowest total valence of Cu and the biggest partial charge (ΔQ_{CO}) accommodated on CO. The structures exhibiting lower CO stretching frequency can be identified as {CuCO}¹⁰ attached to a silanol and a siloxy group that are in vicinal (Figure 3a,e,g) or adjacent position (Figure 3i). Obviously, ΔQ_{CO} is correlated with the d_{CO} values for the optimized structures, but for oxidized CO, one can expect strengthening of the bond and an upward shift of CO oscillation frequency. The reverse situation indicates unequal contributions of σ donation and π back-donation in the bonding mechanism. Although the net charge of CO is positive, the π^* antibonding

system has been populated sufficiently to reproduce the observed experimental features.

The partitioning of the total density of states (DOS) into atomic and orbital contributions presented in Figure 6 allows for elucidation of the contributions of both σ and π^* of CO and both d_σ and d_π of Cu. At first, the total DOS of bare sites (not shown) have indicated that for Cu^I–**5T** the valence band of silica support, composed mainly of 2p oxygen levels, spans over a range of -12.7 eV \div -3 eV and -2.4 eV \div -1.2 eV where it overlaps with the fully occupied d-electron band (from -4.5 to -1 eV). In the case of the Cu^{II}–**5T** site, the partially empty d band ranges from -4.3 to 0.7 eV, while the silica valence band ranges from -10 to 0.6 eV (all values with respect to the appropriate E_F levels). In the left panel of Figure 6, projected DOS plots of Cu^I–**5T** and {CuCO}¹⁰–**5T** are shown. Above Fermi level (E_F), strong interaction of $2\pi^*$ of CO with copper d orbitals is confirmed by overlap of orbital-projected DOS which reveals dominant π back-contribution in Cu–CO bonding. In the right panel, illustrating the electronic structure of {CuCO}⁹–**5T**, one can see considerable overlap of $2s + 2p_z$ (σ) orbitals of CO with d orbitals in the occupied and virtual space that opposes the π^* contribution. As a result, the calculated CO stretching frequency tends to be blue-shifted with respect to the free molecule value.

However, another factor has influenced additionally the calculated positive shift of the CO vibration, namely, the positive charge of the Cu^{II}–silica complexes. Calculations for the neutral Cu^{II} carbonyl adducts accommodated by the same silica models but with two siloxy ligands evidenced quantitatively the effect of the charge of the complex. For the neutral {CuCO}⁹–**2T** complex, $\nu_{\text{CO}} = 2138$ cm⁻¹, in the **3T** site, $\nu_{\text{CO}} = 2150$ cm⁻¹, and in **5T** and in **6T**, $\nu_{\text{CO}} = 2140$ cm⁻¹. These values are very close to the free CO molecule frequency and suggest that the experimentally observed blue shift upon adsorption on Cu^{II} originates both from σ overlap and the enhanced electrophilicity of the metal center. This result is in agreement with recent theoretical calculations obtained for {NiCO}⁸–silica⁴⁰ and {MoCO}¹–silica³⁸ where the positive shift of the stretching CO

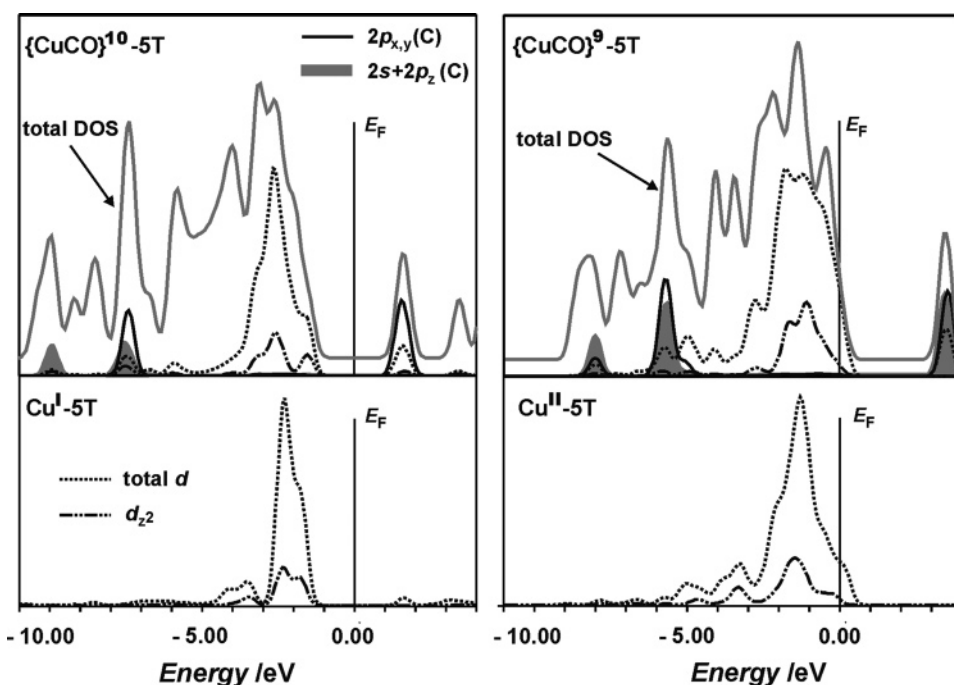


Figure 6. Calculated orbital and atomic projected DOS plots for bare and copper–CO adducts in the **5T** site. The total DOS for adsorbate complexes are shifted upward and scaled by 0.5 ({CuCO}¹⁰) and 0.3 ({CuCO}⁹). E_F is the Fermi level.

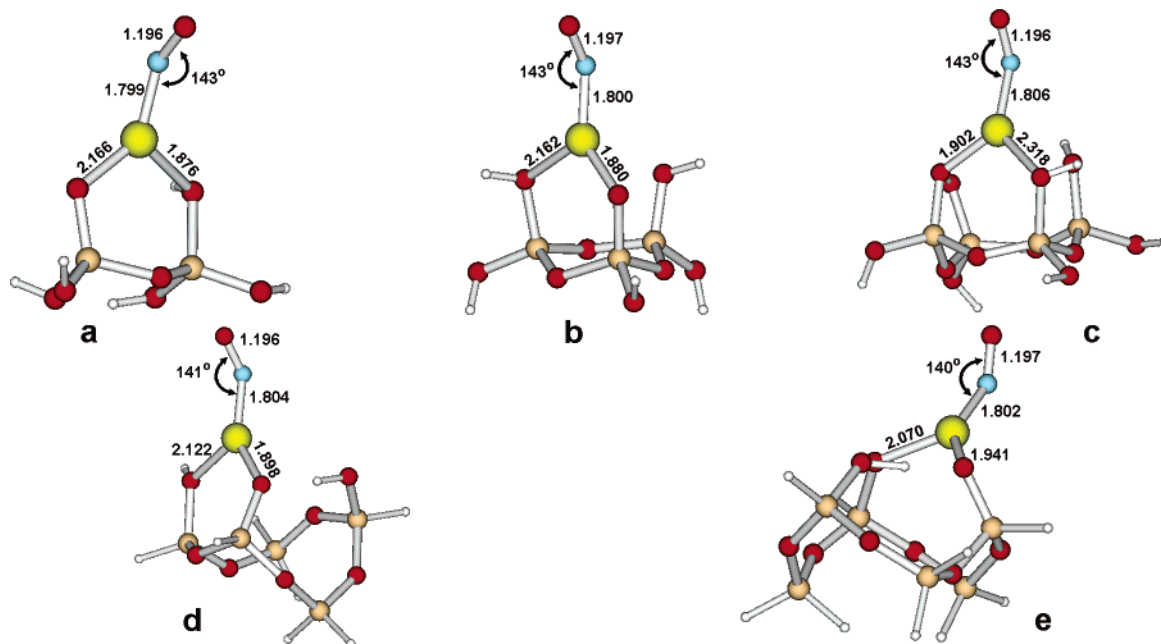


Figure 7. Structures of the mononitrosyl $\{\text{CuNO}\}^{11}$ adsorption complexes nested in the **2T** (a), **3T** (b), **4T** (c), **5T** (d), and **6T** (e) sites. All bond lengths are given in angstroms, and angles, in degrees.

TABLE 7: Comparison of NO Bond Lengths, Adsorption Energies, Selected Population Analysis Data, and NO Stretching Frequency for Cu^I Mononitrosyl $\{\text{CuNO}\}^{11}$ Adducts

	structure			
	$\{\text{CuNO}\}^{11}\text{--}2\text{T}$	$\{\text{CuNO}\}^{11}\text{--}3\text{T}$	$\{\text{CuNO}\}^{11}\text{--}5\text{T}$	$\{\text{CuNO}\}^{11}\text{--}6\text{T}$
ΔE_{ads} (kcal/mol)	−27.9	−27.5	−25.9	−36.1
ΔQ_{Cu}	0.074	0.055	0.117	0.122
ΔQ_{NO}	−0.059	−0.059	−0.040	−0.049
d_{NO}^a (Å)	1.196	1.197	1.196	1.197
N–O bond order ^b	2.065	2.066	2.078	2.070
Cu–N bond order	1.041	1.040	1.026	1.015
Cu total valence	2.398	2.418	2.359	2.325
ν (cm ^{−1}) (<i>int.</i> km/mol)	1753 (496.30)	1753 (495.33)	1756 (495.73)	1748 (515.55)

^a To be compared with 1.179 Å for a free NO molecule. ^b To be compared with a 2.142 bond order for free NO.

frequency could mainly be accounted for by the electrostatic interaction of the ionic charge leading to a change in the polarization of the molecular orbitals of CO.

With regard to the $\{\text{Cu}(\text{CO})_2\}^{10}\text{--nT}$ complexes, vibrational analysis reveals well separated symmetrical and antisymmetrical stretching frequencies characteristic for geminal adducts. The calculated values listed in Table 6 show very good agreement with the available experimental data. In particular, for the **6T** site, an accuracy of less than 6 cm^{−1} has been achieved. The relatively narrow range of calculated frequencies, $\Delta\nu_{\text{symm}} = 15$ cm^{−1} and $\Delta\nu_{\text{asymm}} = 19$ cm^{−1}, suggests homogeneity of the adducts as reflected by only one set of experimental ν_{CO} values.

3.4. Adsorption of NO on Cu/SiO₂. **3.4.1. Structure of Adducts.** The interaction of NO with copper–silica sites has been examined for all types of Cu^I and Cu^{II} clusters. In the case of the Cu^I–**nT** complexes forming the $\{\text{CuNO}\}^{11}\text{--nT}$ adducts, the NO adsorption energies of about −27 kcal/mol are characteristic for **nT** sites with **n** up to 5. For the Cu^I–**6T** complex, the much higher value (−36 kcal/mol) should rather be traced back to the relaxation of the biggest and the most flexible silica model rather than to the formation of the adsorbate complex itself. A similar, but less pronounced effect has already been observed for the $\{\text{CuCO}\}^{10}\text{--6T}$ adduct (compare Table 4). Optimized structures of NO with Cu^I–**nT** surface complexes are depicted in Figure 7, and the adsorption energies (ΔE_{ads}) along with bonding parameters are listed in Table 7. NO

adsorption leads to partial oxidation of the copper centers, as evidenced by the charge distribution. ΔQ_{NO} , a change of the NO partial charge with respect to the free molecule, indicates parallel reduction of the adsorbate. After adsorption, the structures of the resulting adsorption complexes are very similar regardless of the type of the original copper sites; however, the coordination environment of Cu^I changes significantly. All structures exhibit the following generic binding scheme: (i) the Cu^I coordination is planar with CN = 3 (the sum of angles around copper is in the range 359–360°), (ii) Cu^I binds to two framework O atoms, one of which comes from a silanol group, the other from a siloxy group (the silanol and siloxy are in a vicinal position except from the **6T** structure (Figure 7e), where an adjacent placing is observed), (iii) NO is bound angularly to form the $\eta^1\text{--N}$ bent adduct with the Cu–N–O angle (α) in the range 140–143°. A very similar binding picture was obtained for the Cu⁺–NO adducts attached to the MFI framework.⁴⁴ For all adsorbate structures considered, the $d_{\text{Cu--O}}$ bond lengths with silanol groups turn up in the range 2.070–2.318 Å and they are longer than that with silanolate groups, 1.876–1.941 Å. The overall average Cu–O distance ($\langle d_{\text{Cu--O}} \rangle$) increased by about 6% when compared to the bare Cu^I–**nT** models.

The $\{\text{CuNO}\}^{11}$ unit is also very similar for all complexes. The $d_{\text{Cu--N}}$ bond lengths are in the range 1.799–1.806 Å. For the N–O bonds, $d_{\text{N--O}}$ is equal to 1.197 Å, that is, about 0.018 Å longer than that calculated in the free NO. In

TABLE 8: Comparison of NO Bond Lengths, Adsorption Energies, Selected Population Analysis Data, and NO Stretching Frequency for Cu^{II} Mononitrosyl {CuNO}¹⁰ Adducts

	structure			
	{CuNO} ¹⁰ – 2T	{CuNO} ¹⁰ – 3T	{CuNO} ¹⁰ – 5T	{CuNO} ¹⁰ – 6T
ΔE_{ads} (kcal/mol)	–41.2	–41.0	–30.0	–21.7
ΔQ_{Cu}	–0.091	–0.075	–0.025	–0.029
ΔQ_{NO}	0.300	0.312	0.291	0.293
d_{NO}^a (Å)	1.153	1.150	1.152	1.151
N–O bond order ^b	2.103	2.130	2.150	2.171
Cu–N bond order	1.106	1.103	1.039	1.029
Cu total valence	2.839	3.012	2.967	2.969
ν (cm ^{–1}) (int. km/mol)	1931 (841.06)	1933 (959.03)	1913 (841.06)	1919 (864.79)
ν_{NO} experimental ^c	1892			

^a To be compared with 1.179 Å for a free NO molecule. ^b To be compared with a 2.142 bond order for free NO. ^c Experimental data taken from ref 24.

agreement with this, the NO vibrational frequencies, listed in Table 7, are in a narrow range for all the structures (1748–1756 cm^{–1}) and compared to the free NO value (1876 cm^{–1}) are shifted downward by 120–128 cm^{–1}. There have been no experimental data found concerning the NO stretching frequencies on the Cu^I/silica system, since they are very unstable and at low temperatures dimer forms predominate. However, the ΔE_{ads} values suggest thermodynamical stability of the {CuNO}¹¹–silica adduct, and providing sufficiently low pressure of the adsorbate, mononitrosyls could be observed experimentally. The calculated NO valence frequencies are slightly lower than that observed for the {CuNO}¹¹ moieties in the ZSM-5 zeolite.⁶⁶

Contrary to the planar {CuNO}¹¹–**nT** adducts, the products of the adsorption of NO on Cu^{II}–**nT** sites exhibit tetrahedral coordination of Cu(II) with the exception of the **2T** site. Three representatives of the {CuNO}¹⁰–**nT** adducts are presented in Figure 5d–f, while their selected bonding parameters are summarized in Table 8. Adsorption of NO is exoenergetic and leads to the partial reduction of the copper charge with mutual oxidation of the nitrosyl ligand, as evidenced by the ΔQ_{Cu} and ΔQ_{NO} values. Upon NO adsorption, for the **5T** and **6T** sites where copper(II) remained essentially planar before adsorption, local surroundings of Cu^{II} change to pyramidal with the angularly bounded NO in an apical position. For all structures, CN increased due to the addition of the fourth ligand. The average $\langle d_{\text{Cu–O}} \rangle$ distance increases by about 3% when compared to the bare Cu^{II}–**nT** sites. The Cu–N distances range from 1.769 Å (**2T**) to 1.828 Å (**6T**), and the Cu–N bond orders assessed for {CuNO}¹⁰ complexes are slightly higher than those calculated for the {CuNO}¹¹ complexes. A similar observation is valid for the N–O bond, that upon coordination to the copper(II) is reinforced, but here changes are more pronounced. Regardless of the site, the $d_{\text{N–O}}$ values are similar and turn up in the range 1.150–1.153 Å. The bending angles Cu–N–O are in the range 137–148°, similar to the ones of the {CuNO}¹¹ moieties.

Strengthening of the N–O bond is reflected in the calculated NO stretching frequencies. The highest value 1933 cm^{–1} is obtained for the {CuNO}¹⁰–**3T** adduct, and the lowest value 1913 cm^{–1}, for the {CuNO}¹⁰–**5T** adduct; in agreement with the experimental data, they are blue-shifted with respect to the free NO. The calculated positive shift is slightly exaggerated, but the discrepancy is in the range of 2% of the calculated stretching frequency value.

3.4.2. Spectroscopic Features of Adducts. The different IR features of the {CuNO}¹¹ and {CuNO}¹⁰ species can be at best unrevealed with help of the DOS plots. In Figure 8a, a projected atomic and orbital DOS with respect to the Fermi energy (E_{F}) is shown for {CuNO}¹⁰–**5T**. The lower panel (Figure 8b) represents the {CuNO}¹¹–**5T** complex. In the vicinity of the

Fermi level in Figure 8a, strong overlap of the 2s + 2p_z (σ) orbitals of NO with d orbitals indicates a σ -donating effect that, as a consequence, can contribute to the calculated blue shift of the NO stretching frequency on Cu^{II}–**5T**. As it has been pointed out in the case of the {CuCO}⁹ adducts, the net charge of the complex has a considerable influence on the calculated frequency shift. Cooperation of these two effects has resulted in a correct reproduction of the NO shift, since the ν_{NO} values for the neutral complexes have been equal to 1882 cm^{–1} ({CuNO}¹⁰ in the **2T** site), 1876 cm^{–1} (for the **3T** site), 1847 cm^{–1} (**4T**), and 1836 cm^{–1} (for the **5T** site). The effect of the charge is more pronounced for the nitrosyl complexes than for the carbonyl ones. This might be traced back to the lower energy of the frontier orbitals of NO (in comparison with CO) which makes it more prone to the changes in electron donor–acceptor properties of the adsorption site. On the contrary, for the {CuNO}¹¹–**5T** complex, the Fermi level is dominated by π^* of NO. Its interaction with filled d_π of Cu leads to the dominant π back-contribution in Cu⁺–NO bonding and consequent lowering of the ν_{NO} value with respect to the free NO.

Since there are no experimental data available on the {CuNO}¹¹–silica complex so far, its electronic and magnetic

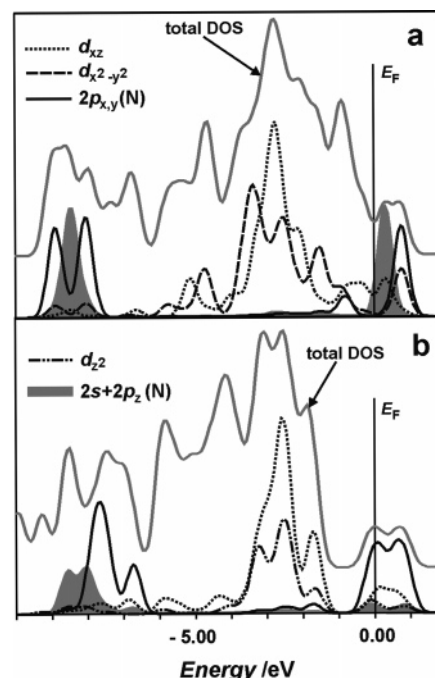


Figure 8. Calculated total, orbital, and atomic projected DOS plots for {CuNO}¹⁰ (a) and {CuNO}¹¹ (b) adducts in the **5T** site. Total DOS plots are scaled by 0.2 and shifted upward. E_{F} is the Fermi level.

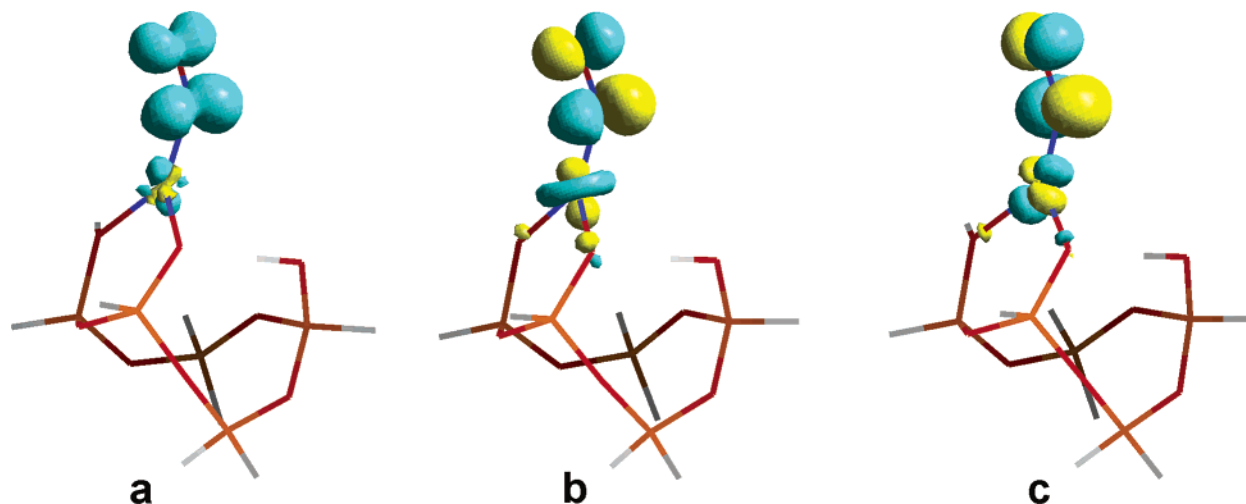


Figure 9. Calculated spin density (a), SOMO (b), and LUMO (c) contours for the $\{\text{CuNO}\}^{11}\text{-5T}$ complex.

TABLE 9: Spin Density Properties of the $\{\text{CuNO}\}^{11}\text{-5T}$ Adsorption Complex and Comparison with the ZSM-5 Zeolite-Encaged $\{\text{CuNO}\}^{11}$ Magnetophore

observable	$\{\text{CuNO}\}^{11}\text{-5T}$	$\{\text{CuNO}\}^{11}\text{-M5(7)}^a$	$\text{Cu}^{\text{I}}\text{-NO/ZSM-5}^b$
$^{\text{Cu}}a_{\text{iso}}, ^{\text{Cu}}T_{ii}$ (10^{-4} cm $^{-1}$)	230.8/−6.5/−18.1/24.6	158.7/−4.1/−19.0/23.1	158.5/−9.0/−13.6/22.6
$^{\text{N}}a_{\text{iso}}, ^{\text{N}}T_{ii}$ (10^{-4} cm $^{-1}$)	12.2/17.9/−9.4/−8.5	11.7/19.1/−9.8/−9.3	12.3/15.7/−8.3/−7.4
g_{ii}	2.013/2.026/1.887	2.001/2.034/1.883	1.999/2.003/1.889
$^{\text{Cu}}\rho, ^{\text{N}}\rho, ^{\text{O}}\rho$	0.08, 0.56, 0.35	0.12, 0.56, 0.35	0.16, 0.54, 0.30

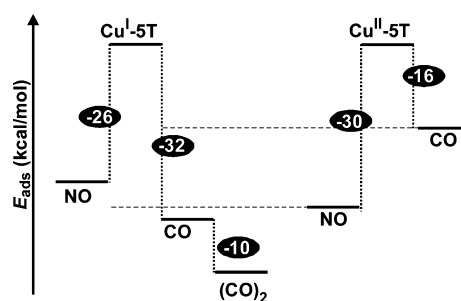
^a From ref 44. ^b From ref 68.

structure can be approached in a computational manner, taking into account the complementarity between theory and experiment evidenced in this study. Closer inspection of the orbital-projected DOS for $\{\text{CuNO}\}^{11}\text{-5T}$ in the vicinity of the Fermi level unravels a complicated nature of the $\text{Cu}^+\text{-NO}$ bonding mechanism. For this open-shell radical complex, the unpaired electron density is delocalized over $2p_{x,y}(\text{N})$ (π^*) with considerable contributions of d_{z^2} and d_{xz} (Figure 8b). The composition of the SOMO and LUMO orbitals along with the spin density contour for $\{\text{CuNO}\}^{11}\text{-5T}$ is depicted in Figure 9. To facilitate description, according to the generic binding scheme presented above, for the $\text{ON-Cu}^+\{(\text{OSi})_2\}_{\text{sil}}$ adducts, we can discuss the electronic properties in terms of the C_s microsymmetry, with the mirror plane defined by the Cu, N, and O atoms. In such a frame, the SOMO is composed of the in-plane a' orbitals $\pi^*(2p_x)$, d_{xz} , and d_{z^2} and a lone pair of NO, whereas the LUMO is an orthogonal a'' symmetry species composed of $\pi^*(2p_y)$ and d_{yz} . The tilting of the NO ligand improves the overlap between copper $3d_{z^2}$ and $\pi^*(2p_x)$ of the NO molecule.⁶⁷ Moreover, bending enables the overlap between $4s$ of Cu and $\pi^*(2p_x)$ of NO which is not allowed in the linear mode of the NO ligation. This mechanism is in total analogy of the electronic picture of the $\{\text{CuNO}\}^{11}$ moiety inside the ZSM-5 zeolite shown previously⁴⁴ and with the interpretation of its experimental spectrum.⁶⁸ The direct indication of the $4s$ contribution in the SOMO can be found within the results of the hyperfine coupling constant calculations. These data, isotropic a_{iso} and anisotropic dipolar T_{ii} hyperfine coupling constants, along with the g -tensor results are listed in Table 9. The most characteristic feature is a big positive value of the $^{\text{Cu}}a_{\text{iso}}$ parameter. This can only be explained by the direct delocalization of the spin density over the copper $4s$ orbital. This effect is similar, but to a greater extent, to the $\{\text{CuNO}\}^{11}$ moiety inside the ZSM-5. In fact, all tensors, $^{\text{Cu}}A$, $^{\text{N}}A$, and g , indicate similar character of the $\{\text{CuNO}\}^{11}$ unit on both catalytic surfaces, SiO₂ and ZSM-5. Probably the main reason of such a behavior is a confinement of the spin density to the $\{\text{CuNO}\}^{11}$ unit, as shown in Figure

9a. Such moieties, bearing the magnetic properties of the whole system, can be named magnetophores.⁶⁹

3.5. Coadsorption of CO and NO. In the studies of coadsorption of NO and CO on a Cu/SiO₂ catalyst^{24,26} and other micro- and mesoporous copper-containing materials,^{11,70,71} it has been concluded that adsorption of a CO/NO mixture allows simultaneous and selective detection of the Cu^{I} and Cu^{II} cations. At room temperature, CO molecules are preferably adsorbed on the Cu^{I} -silica sites, whereas NO molecules adsorb strongly on the Cu^{II} -silica sites. The presented work corroborates this observation. The adsorption energies of all studied surface species for the **5T** model are collected in Scheme 1. Even though the differences between particular values are not big (compare adsorption of NO and CO on $\text{Cu}^{\text{I}}\text{-5T}$), they give rise to the discrimination between adsorbate complexes formed. According to the Boltzmann distribution, the adsorption energies for the $\text{Cu}^{\text{I}}\text{-5T}$ cluster at 298 K result in a fraction of CO occupied to NO occupied sites equal to $N_{\text{CO}}/N_{\text{NO}} = 2 \times 10^4$. For the $\text{Cu}^{\text{II}}\text{-5T}$ cluster, selectivity of the adsorption is even greater and $N_{\text{NO}}/N_{\text{CO}} = 3 \times 10^{10}$. Therefore, in the CO/NO reaction atmosphere, the mixture of $\{\text{CuNO}\}^{10}$ and $\{\text{CuCO}\}^{10}$ as well as $\{\text{Cu}(\text{CO})_2\}^{10}$ silica-supported species is expected.

SCHEME 1: Comparison of the Interaction Energies (in kcal/mol) for the Adsorption of CO and NO Molecules on the $\text{Cu}^{\text{I}}\text{-5T}$ and $\text{Cu}^{\text{II}}\text{-5T}$ Sites



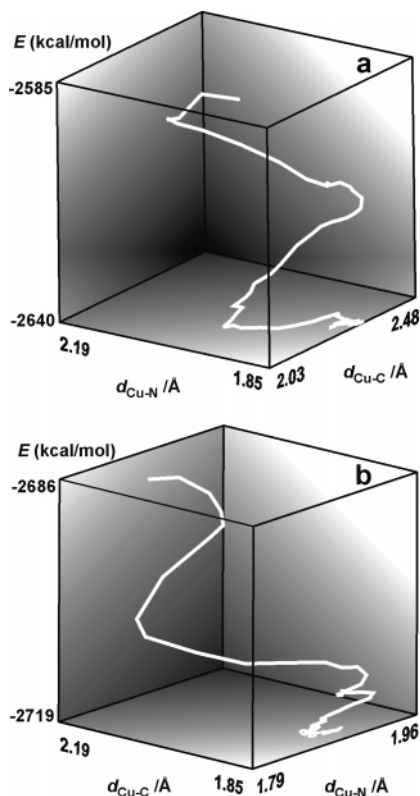


Figure 10. Optimization pathways for the reaction of $\{\text{CuNO}\}^{10}$ with a CO molecule (a) and $\{\text{CuNO}\}^{11}$ with a CO molecule (b) as a function of SCF energy in Cu–C and Cu–N coordinates (for details, see text).

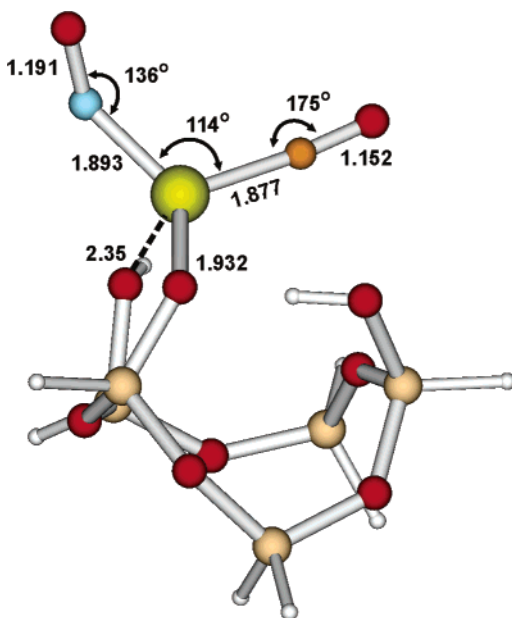


Figure 11. Optimized structure of the mixed-ligand carbonyl nitrosyl Cu^{I} complex attached to the 5T site. All bond lengths are given in angstroms, and angles, in degrees.

To check the possibility of the formation of a mixed-ligand complex, the products of the following reactions have been investigated: (1) $\{\text{CuNO}\}^{11}-5\text{T} + \text{CO}$ and (2) $\{\text{CuNO}\}^{10}-5\text{T} + \text{CO}$. For each of the optimized mononitrosyl complex structures, a CO molecule has been attached at a distance equal to 2 Å and the structures have been fully optimized. The resulting optimization pathways plotted against $d_{\text{Cu-N}}$, $d_{\text{Cu-C}}$, and SCF energy coordinates are depicted in Figure 10. For the $\text{Cu}^{\text{II}}-5\text{T}$ site (Figure 10a), the CO molecule has been moved

away from copper at the distance ~ 2.4 Å, while the Cu–N distance remained almost unchanged. A different situation has been observed for the $\text{Cu}^{\text{I}}-5\text{T}$ site (Figure 10b) where the mixed-ligand complex $\{\text{Cu}(\text{CO})(\text{NO})\}^{11}-5\text{T}$ is formed. The Cu–C distance drops rapidly to reach the value $d_{\text{Cu-C}} = 1.877$ Å. The adsorption energy of CO is equal to -11.9 kcal/mol, and the resulting structure is shown in Figure 11. The CO molecule is bonded at the expense of the Cu–silanol link in almost linear mode. When comparing to the $\{\text{CuNO}\}^{11}-5\text{T}$ and $\{\text{CuCO}\}^{10}-5\text{T}$ adducts, the changes in geometry consist mainly of an increase of the Cu–N and Cu–C bond lengths by about 0.09 Å, but the lengthening of the intermolecular ligands' bonds does not exceed 0.005 Å. Spin density is still localized within the $\{\text{CuNO}\}^{11}$ moiety (95% of the total spin), and the calculated stretching frequencies, well separated from each other, are very close to the ones obtained for parent $\{\text{CuNO}\}^{11}-5\text{T}$ and $\{\text{CuCO}\}^{10}-5\text{T}$ adducts, and equal to $\nu_{\text{CO}} = 2124$ cm^{-1} and $\nu_{\text{NO}} = 1724$ cm^{-1} . Therefore, although a higher preference to the formation of $\{\text{CuCO}\}^{10}$ on reduced catalyst than the $\{\text{CuNO}\}^{11}$ is confirmed on the basis of ΔE_{ads} , the frequency characteristic for NO adsorbed on the Cu^{I} might appear not as a result of the $\{\text{CuNO}\}^{11}$ formation but as a feature of the mixed-ligand silica-supported complex of the $\{\text{Cu}(\text{CO})(\text{NO})\}^{11}$ type.

4. Conclusions

In this work, various framework model clusters, cut off from the real amorphous surface, have been investigated to mimic the local environment of the isolated copper sites on the Cu/SiO₂. The present study revealed the possibility of the existence of isolated Cu^{I} and Cu^{II} ions in various surroundings on the surface of the amorphous silica. These sites differ in a number of ligands that are attached to the metal. Cu^{II} ions show 3-fold coordination with the g -tensors of high anisotropy. Reduced sites are exclusively two-coordinated. Adsorption of CO molecules is found to be stronger on the reduced sites than on the $\text{Cu}^{\text{II}}-\text{nT}$. The reverse trend is observed for the NO adsorption. The differences in adsorption energies are sound enough to predict selective adsorption from the CO/NO mixture on the basis of Boltzmann distribution. However, in the case of the $\text{Cu}^{\text{I}}-\text{nT}$ sites, formation of a mixed-ligand complex with one CO molecule and one NO molecule is predicted. For all adsorbate complexes, the vibrational analysis gives the stretching frequencies in very good agreement with the available experimental counterparts. A positive shift of the stretching frequency from the free molecule values is calculated for the CO and NO adducts on the $\text{Cu}^{\text{II}}-\text{nT}$ sites, whereas for the $\text{Cu}^{\text{I}}-\text{nT}$ sites monocarbonyl adducts exhibit a negative shift. Two factors enter to successfully account for these observations: redistribution of the electron density within σ and π systems of the adsorbates revealed by orbital-projected DOS analysis and, in the case of divalent adducts, enhanced electrophilicity of the supported copper ion mimic by positively charged models. Successive adsorption of the second CO molecule leads to the very uniform geminal dicarbonyl structure regardless of the reduced site. Calculated frequencies of symmetrical and antisymmetrical vibrations corroborate the experimental values.

Acknowledgment. Support by the Polish State Committee for Scientific Research (KBN), project number 3 T09A 147 26, is acknowledged. The calculations were performed with the computer facilities of CYFRONET-AGH, Grant No. KBN/SGI2800/UJ/018/2002. This paper is dedicated to Marek Nocoń, a friend of mine.

References and Notes

- (1) Brown, G. E.; Henrich, V. E.; Casey, W. H.; Clark, D. L.; Eggleston, C.; Felmy, A.; Goodman, D.; WayneGratzel, M.; Maciel, G.; McCarthy, M. I.; Nealon, K. H.; Sverjensky, D. A.; Toney, M. F.; Zachara, J. M. *Chem. Rev.* **1999**, 99, 77.
- (2) *Applied Homogeneous Catalysis with Organometallic Compounds*; Cornils, B., Herrmann, W. A., Eds.; VCH: Weinheim, Germany, 1996.
- (3) *Handbook of Heterogeneous Catalysis*; Ertl, G., Knözinger, H., Weitkamp, J., Eds.; Wiley-VCH: Weinheim, Germany, 1997.
- (4) Shelef, M. *Chem. Rev.* **1995**, 95, 209.
- (5) Stamler, J.; Singel, D. J.; Loscalzo, J. *Science* **1992**, 259, 1989.
- (6) Parton, R. F.; Vankelecom, I. F. J.; Casselman, M. J. A.; Bezoukhanova, C. P.; Uytterhoeven, J. B.; Jacobs, P. A. *Nature* **1994**, 370, 541.
- (7) Kobayashi, H.; Takezawa, N.; Minochi, C. *J. Catal.* **1981**, 69, 487.
- (8) Ossipoff, N. J.; Cant, N. W. *J. Catal.* **1994**, 148, 125.
- (9) De Sousa, E. M. B.; Guimaraes, A. P.; Mohallem, N. D. S.; Lago, R. M. *Appl. Surf. Sci.* **2001**, 183, 216.
- (10) Guo, X. F.; Lai, M.; Kong, Y.; Ding, W. P.; Yan, Q. *J. Langmuir* **2004**, 20, 2879.
- (11) Tsoncheva, T.; Venkov, Tz.; Dimitrov, M.; Minchev, C.; Hadjiivanov, K. *J. Mol. Catal. A: Chem.* **2004**, 209, 125.
- (12) Shen, J. G. C. *J. Phys. Chem. B* **2004**, 108, 44.
- (13) Jin, A. Z.; Wang, Y. G.; Zhang, Z. *J. Cryst. Growth* **2003**, 252, 167.
- (14) Espinos, J. P.; Morales, J.; Barranco, A.; Caballero, A.; Holgado, J. P.; Gonzalez-Elipe, A. R. *J. Phys. Chem. B* **2002**, 106, 6921.
- (15) van den Oetelaar, L. C. A.; Partridge, A.; Toussaint, S. L. G.; Flipse, C. F. J.; Brongersma, H. H. *J. Phys. Chem. B* **1998**, 102, 9541.
- (16) van den Oetelaar, L. C. A.; Partridge, A.; Stapel, P. J. A.; Flipse, C. F. J.; Brongersma, H. H. *J. Phys. Chem. B* **1998**, 102, 9532.
- (17) Wang, Z.; Liu, Q.; Yu, J.; Wu, T.; Wang, G. *Appl. Catal., A* **2003**, 239, 87.
- (18) Trouillet, L.; Toupance, T.; Villain, F.; Louis, C. *Phys. Chem. Chem. Phys.* **2000**, 2, 2005.
- (19) Toupance, T.; Kermarec, M.; Lambert, J. F.; Louis, C. *J. Phys. Chem. B* **2002**, 106, 2277.
- (20) Cheah, S.-F.; Brown, G. E., Jr.; Parks, G. A. *J. Colloid Interface Sci.* **1998**, 208, 110.
- (21) Kuroda, Y.; Yoshikawa, Y.; Yuzo, K.; Kumashiro, R.; Nagao, M. *J. Phys. Chem. B* **1997**, 101, 6497.
- (22) Busca, G. J. *Mol. Catal.* **1987**, 43, 225.
- (23) Hadjiivanov, K.; Venkov, T.; Knözinger, H. *Catal. Lett.* **2001**, 75, 55.
- (24) Hadjiivanov, K.; Knözinger, H. *Phys. Chem. Chem. Phys.* **2001**, 3, 1132.
- (25) Pietrzyk, P.; Sojka, Z.; Gil, B.; Datka, J.; Broclawik, E. *Stud. Surf. Sci. Catal.* **2002**, 142, 453.
- (26) Hadjiivanov, K. *Catal. Rev.—Sci. Eng.* **2000**, 42, 71.
- (27) Legrand, A. P. In *The Surface Properties of Silica*; Legrand, A. P., Ed.; Wiley: Chichester, U.K., 1998.
- (28) Iler, R. K. *The Colloid Chemistry of Silicates*; Cornell University Press: Ithaca, NY, 1955.
- (29) Hsu, L. Y.; Shore, S. G.; D'Ornelas, L.; Choplin, A.; Basset, J. M. *J. Catal.* **1994**, 149, 159.
- (30) Ma, Q.; Klier, K.; Cheng, H.; Mitchell, J. W. *J. Phys. Chem. B* **2002**, 106, 10121.
- (31) Sierka, M.; Sauer, J. *Faraday Discuss.* **1997**, 106, 41.
- (32) Lopez, N.; Pacchioni, G.; Maseras, F.; Illas, F. *Chem. Phys. Lett.* **1998**, 294, 611.
- (33) Ma, Q.; Klier, K.; Cheng, H.; Mitchell, J. W.; Hayes, K. S. *J. Phys. Chem. B* **2000**, 104, 10618.
- (34) Sokol, A. A.; Catlow, C. R. A.; Garces, J. M.; Kuperman, A. J. *Phys. Chem. B* **2002**, 106, 6163.
- (35) Feuston, B. P.; Garofalini, S. H. *J. Chem. Phys.* **1989**, 91, 564.
- (36) Garofalini, S. H. *J. Non-Cryst. Solids* **1990**, 120, 1.
- (37) Ricci, D.; Pacchioni, G.; Szymanski, M. A.; Shluger, A. L.; Stoneham, A. M. *Phys. Rev. B* **2001**, 64, 224104.
- (38) Lopez, N.; Illas, F.; Pacchioni, G. *J. Mol. Catal. A: Chem.* **2001**, 170, 175.
- (39) Garrot, J. M.; Lepetit, C.; Che, M.; Chaquin, P. *J. Phys. Chem. A* **2001**, 105, 9445.
- (40) Costa, D.; Martra, G.; Che, M.; Manceron, L.; Kermarec, M. J. *Am. Chem. Soc.* **2002**, 124, 7210.
- (41) Lopez, N.; Illas, F.; Pacchioni, G. *J. Phys. Chem. B* **1999**, 103, 8552.
- (42) Ferullo, F. M.; Castellani, N. J. *J. Mol. Catal. A: Chem.* **2004**, 221, 155.
- (43) Sauer, J.; Ugliengo, P.; Garrone, E.; Saunders, V. R. *Chem. Rev.* **1994**, 94, 2095.
- (44) Pietrzyk, P.; Piskorz, W.; Sojka, Z.; Broclawik, E. *J. Phys. Chem. B* **2003**, 107, 6105.
- (45) Delley, B. *J. Chem. Phys.* **1990**, 92, 508.
- (46) *DMol, InsightII*, release 2000.1; Accelrys Inc.: San Diego, CA, 2000.
- (47) Becke, A. D. *J. Chem. Phys.* **1988**, 88, 2547.
- (48) Perdew, J. P.; Wang, Y. *Phys. Rev. B* **1992**, 45, 13244.
- (49) Schlegel, B. H. In *Ab initio Methods In Quantum Chemistry—II*; Lawley, K. P., Ed.; Wiley: New York, 1987.
- (50) Hirshfeld, F. L. *Theor. Chim. Acta* **1977**, 44, 129.
- (51) Mayer, I. *Int. J. Quantum Chem.*, **1986**, 29, 477.
- (52) Frish, M. J.; et al. *Gaussian03*, revision B.05; Gaussian, Inc.: Pittsburgh, PA, 2003.
- (53) te Velde, G.; Bickelhaupt, F. M.; van Gisbergen, S. J. A.; Fonseca Guerra, C.; Baerends, E. J.; Snijders, J. G.; Ziegler, T. *J. Comput. Chem.* **2001**, 22, 931.
- (54) ADF2002.03, SCM, Theoretical Chemistry, Vrije Universiteit, Amsterdam, The Netherlands (<http://www.scm.com>).
- (55) Schreckenbach, G.; Ziegler, T. *J. Phys. Chem. A* **1997**, 101, 3388.
- (56) Scott, A. P.; Radom, L. *J. Phys. Chem.* **1996**, 100, 16502.
- (57) Pierloot, K.; Delabie, A.; Groothaert, M. H.; Schoonheydt, R. A. *Phys. Chem. Chem. Phys.* **2001**, 3, 2174.
- (58) Berthomieu, D.; Krishnamurty, S.; Coq, B.; Delahay, G.; Goursot, A. *J. Phys. Chem. B* **2001**, 105, 1149.
- (59) Hathway, B. J.; Billing, D. E. *Coord. Chem. Rev.* **1970**, 5, 143.
- (60) Delabie, A.; Pierloot, K.; Groothaert, M. H.; Schoonheydt, R. A.; Vanquickenborne, L. G. *Eur. J. Inorg. Chem.* **2002**, 515.
- (61) Enemark, J. H.; Feltham, R. D. *Coord. Chem. Rev.* **1974**, 13, 339.
- (62) Davidova, M.; Nachtigallova, D.; Bulanek, R.; Nachtigall, P. *J. Phys. Chem. B* **2003**, 107, 2327.
- (63) Suvanto, S.; Hirva, P.; Pakkanen, T. A. *Surf. Sci.* **2000**, 465, 277.
- (64) Zecchina, A.; Bordiga, S.; Turnes Palomino, G.; Scarano, D.; Lamberti, C.; Salvalaggio, M. *J. Phys. Chem. B* **1999**, 103, 3833.
- (65) Rack, J. J.; Webb, J. D.; Strauss, S. H. *Inorg. Chem.* **1996**, 35, 277.
- (66) Broclawik, E.; Datka, J.; Gil, B.; Kozyra, P. *Phys. Chem. Chem. Phys.* **2000**, 2, 401.
- (67) Scheidt, W. R.; Ellison, M. K. *Acc. Chem. Res.* **1999**, 32, 350.
- (68) Sojka, Z.; Che, M.; Giamello, E. *J. Phys. Chem. B* **1997**, 101, 4831.
- (69) Pietrzyk, P.; Sojka, Z. *J. Phys. Chem. B*, submitted for publication.
- (70) Milushev, A.; Hadjiivanov, K. *Phys. Chem. Chem. Phys.* **2001**, 3, 5337.
- (71) Hadjiivanov, K.; Dimitrov, L. *Microporous Mesoporous Mater.* **1999**, 27, 49.